Electronic Supplementary Information

High-entropy layered double hydroxides enabled wide-bandwidth near-infrared photodetection with viable environmental resistance

Kent-Tien Liang[a], Li-Mei Cheng[a], Kai-Lin Hsiao[b], Po-Hsuan Hsiao[b, c], Yi-Ting Li[b], and Chia-Yun Chen[a,b**]

[a]*Program on Semiconductor Packaging and Testing, Academy of Innovative Semiconductor and Sustainable Manufacturing, National Cheng Kung University, Tainan 70101, Taiwan*

[b] *Department of Materials Science and Engineering, National Cheng Kung University, Tainan 70101, Taiwan.*

[c]*Department of Materials Engineering, Ming Chi University of Technology, New Taipei, Taiwan*

*Email: timcychen@mail.ncku.edu.tw

S1 Characteristizations of LDHs

S1-1 XRD patterns, FTIR spectra and Mott Schottky plots

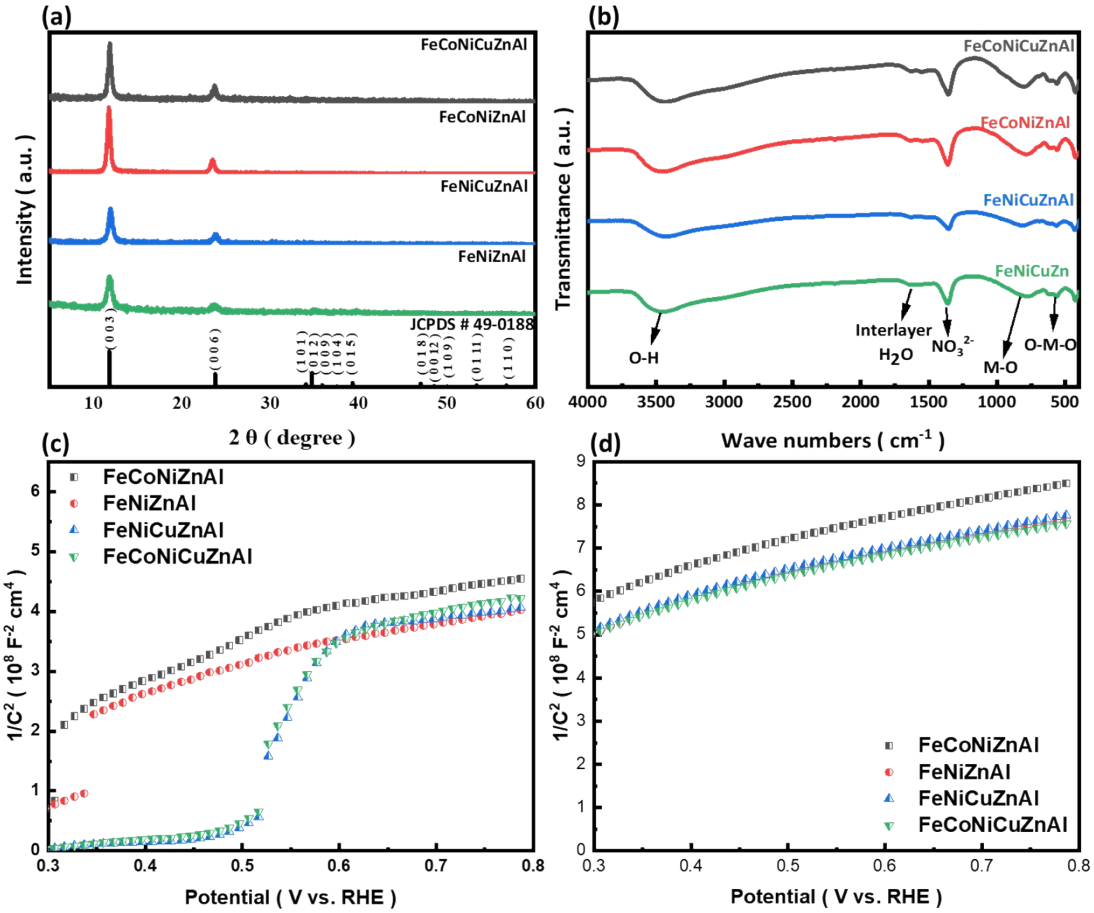

Fig. S1 (a) XRD patterns, (b) FTIR spectra and Mott Schottky plots at (c) low frequencies (1 Hz) and (d) high frequencies (1000 Hz) of FeCoNiCuZnAl-LDH, FeCoNiZnAl-LDH, FeNiCuZnAl-LDH, and FeNiZnAl-LDH, respectively.

The crystallographic patterns of the hydrothermally derived LDH structures were indexed via the XRD investigations, as depicted in Fig. S1(a). The four synthesized LDH structures exhibited the consistent diffraction features of hydrotalcite. In FeCoNiCuZnAl six multi-element constitutes, the partial isovalent replacement of Ni^{2+} with Co^{2+}, Zn^{2+}, and Cu^{2+} cations, accompanied by the partial substitution of Fe^{3+} by Al^{3+} formulated the similar crystallographic closely resembling to the reference of $Fe_2Ni_2CO_3(OH)_8 \cdot 2H_2O$ (JCPDS No. 49-0188). The pronounced reflections at $2\theta = 11.8°$ and 23.7°, assigned to the (003) and (006) lattice planes, respectively, constitute the

diagnostic hallmarks of LDH phase formation, reflecting the periodic stacking of positively charged brucite-like layers interleaved with charge-compensating anions and associated water molecules.

In addition, to probe the chemical functionality and interlayer species within the LDH framework, FTIR analyses were conducted, as illustrated in Fig. S1(b). The extensive absorption envelope centered near 3458 cm^{-1} was ascribed to the stretching vibrations of hydroxyl moieties integral to the LDH lattices[1] , and the distinct band at 1600 cm^{-1} originating from the bending vibrations of interlamellar H_2O molecules was visualized[2]. These features indicated the retained hydrogen-bond interactions between hydroxide layers as LDH crystals were grown. The vibrational feature at 1350 cm^{-1} was attributed to the asymmetric stretching of intercalated NO_3^- groups[3], a direct manifestation of charge-balancing anions derived from the precursor solution and preferentially accommodated between layers. The persistence of NO_3^- signatures correlated with a pronounced growth anisotropy along the (00l) crystallographic axis, consistent with the thermodynamically favored stacking mode of LDHs.

The frequency-dependent Mott–Schottky characteristics at 1 Hz and 1000 Hz were displayed in Figs. S1(c) and S1(d), in which the potential range was intentionally restricted to 0.3–0.8 V to avoid the flat-band interference typically observed below 0.2 V. The explicit differences among the FeCoNiZnAl-, FeNiZnAl-, FeNiCuZnAl-, and FeCoNiCuZnAl-LDH samples were visualized. At low frequencies (1 Hz), the FeCoNiZnAl- and FeNiZnAl-LDHs exhibited an abrupt capacitance enhancement at 0.30–0.35 V followed by a moderate elevation between 0.33 and 0.55 V, which was attributed to the presence of abundant and disordered defect states that induced a broad distribution of interfacial trap energy levels. Such disordered interfacial traps led to inconsistent capacitive responses across this bias region. By contrast, the FeNiCuZnAl- and FeCoNiCuZnAl-LDHs displayed the relatively uniform capacitance rise occurring

near 0.50–0.55 V, which reflected a reduced density and improved ordering of trap states originating from the configurational-entropy–driven homogenization of the local electronic environment. Furthermore, the sharp and continuous capacitance increased observed at 0.55–0.60 V in the FeNiCuZnAl- and FeCoNiCuZnAl-LDHs suggested that the interfacial states were more energetically aligned, consistent with the improved structural uniformity revealed by the GIWAXS and XPS analyses.

S1-2 EDS mapping of synthesized LDHs

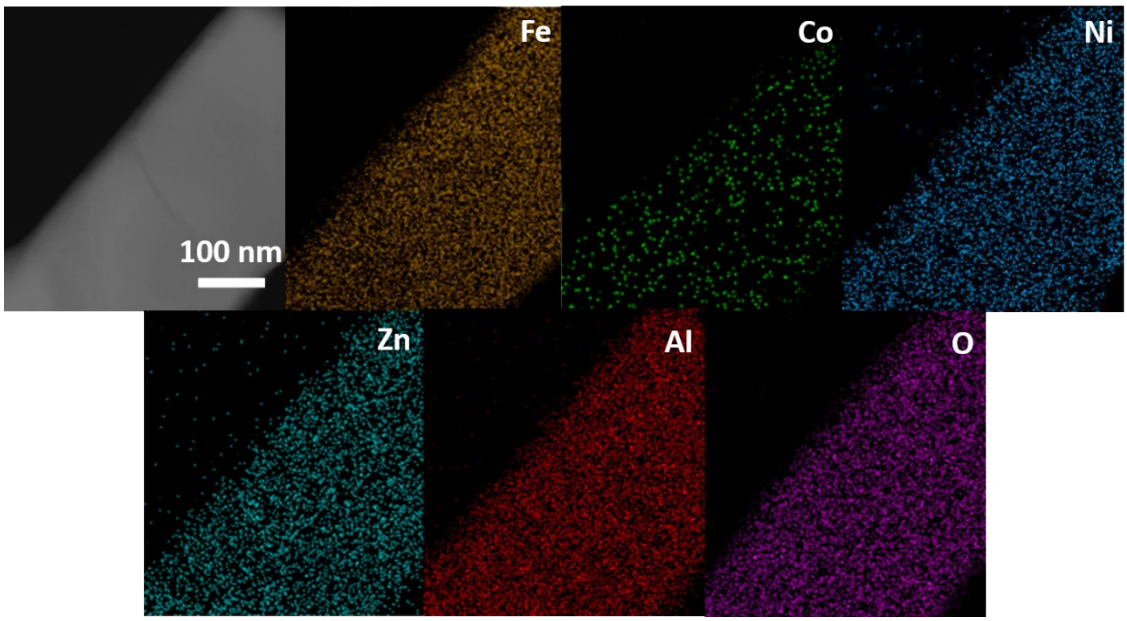

Fig. S2 EDS elemental mapping of FeCoNiZnAl–LDH.

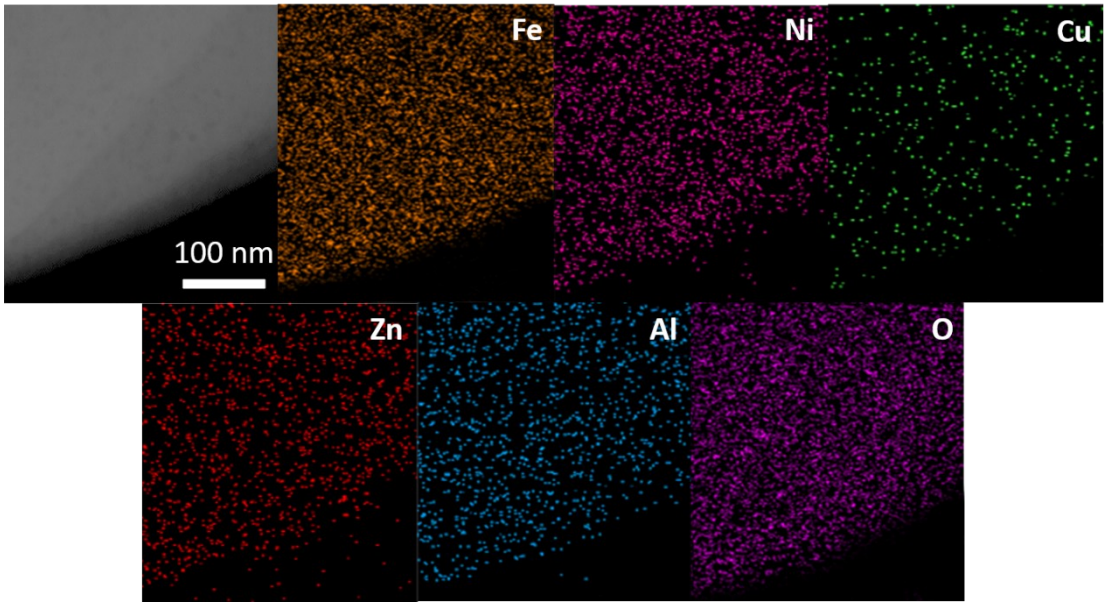

Fig. S3 EDS elemental mapping of FeNiCuZnAl–LDH.

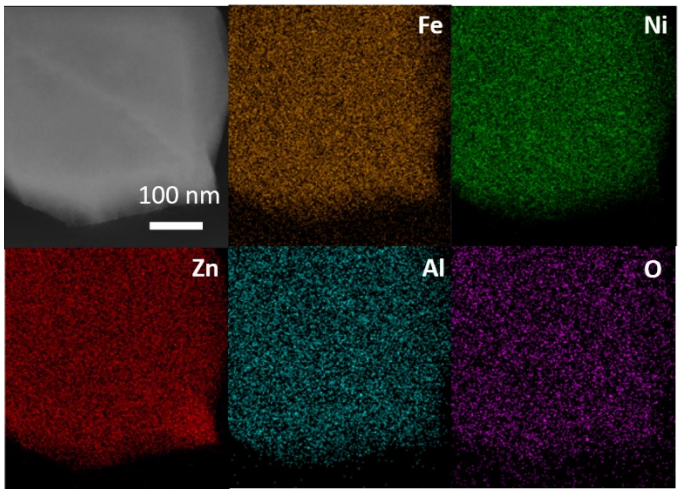

Fig. S4 EDS elemental mapping of FeNiZnAl–LDH.

S1-3 Elemental composition and configuration entropy of synthetic LDHs

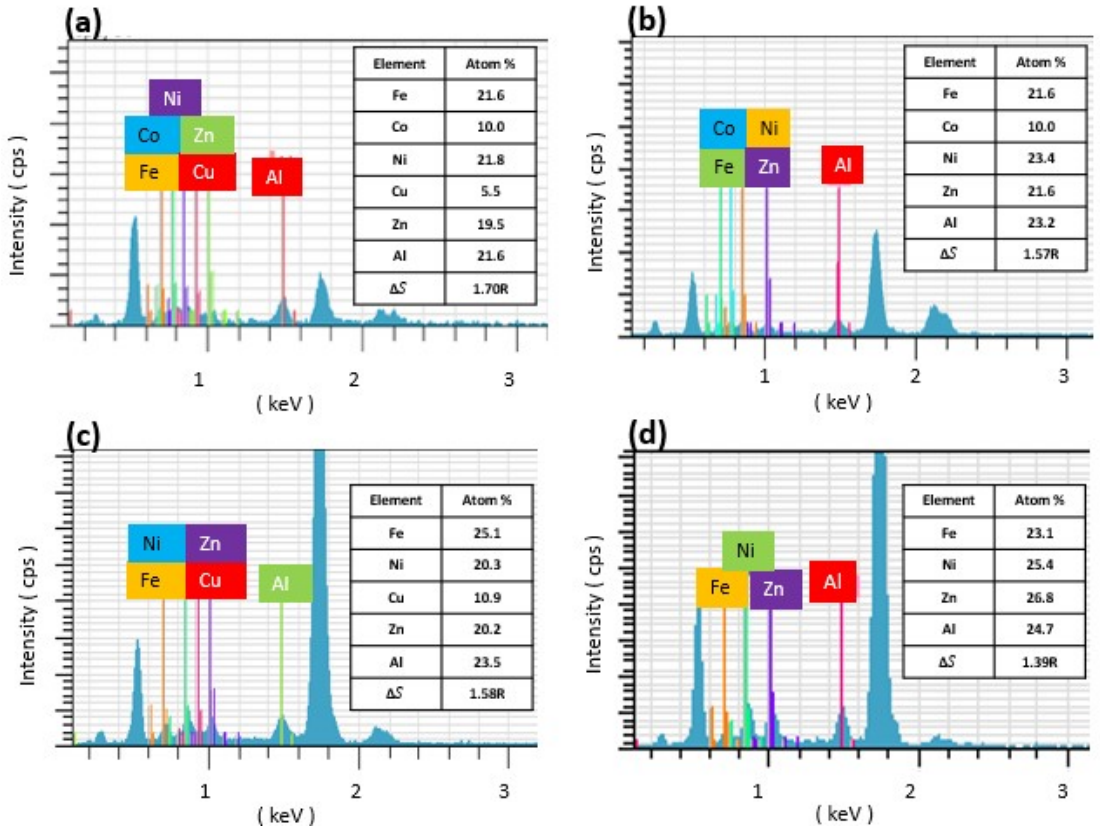

Fig. S5 Quantitative EDS spectra of (a) FeCoNiCuZnAl-LDH, (b) FeCoNiZnAl-LDH, (c) FeNiCuZnAl-LDH, and (d) FeNiZnAl-LDH, respectively.

The EDS spectra unambiguously revealed the incorporation of Fe, Co, Ni, Cu, Zn, and Al into the FeCoNiCuZnAl-LDH lattices, revealing the atomic fractions of Fe (21.6 at%), Co (10.0 at%), Ni (21.8 at%), Cu (5.5 at%), Zn (19.5 at%), and Al (21.6 at%). These values were further corroborated by ICP-MS analysis, which disclosed closely matching atomic percentages of Fe (21.9 at%), Co (10.1 at%), Ni (21.5 at%), Cu (5.1 at%), Zn (20.1 at%), and Al (21.1 at%). The remarkable consonance between these two orthogonal techniques implicates a high degree of compositional fidelity across multiple probing depths, thereby validating both the reproducibility of the hydrothermal synthesis protocol and the intrinsic uniformity of the cationic distribution.

Table S1 Summary of elemental compositions and configuration entropy of FeCoNiCuZnAl-LDH, FeCoNiZnAl-LDH, FeNiCuZnAl-LDH, and FeNiZnAl-LDH estimated from ICP-MS and EDS analyses, respectively.

Atom %		**Fe**	**Co**	**Ni**	**Cu**	**Zn**	**Al**	ΔS
FeCoNiCuZnAl	ICP-MS	21.9	10.1	21.5	5.1	20.1	21.1	1.70R
	EDS	21.6	10.0	21.8	5.5	19.5	21.6	1.70R
FeCoNiZnAl	ICP-MS	22.6	10.8	24.2	-	21.2	21.2	1.57R
	EDS	21.8	10.0	23.4	–	21.6	23.2	1.57R
FeNiCuZnAl	ICP-MS	26.5	-	20.9	11.6	17	24	1.57R
	EDS	25.1	–	20.3	10.9	20.2	23.5	1.58R
FeNiZnAl	ICP-MS	22.2	-	24.4	-	27.3	26.1	1.38R
	EDS	23.1	–	25.4	–	26.8	24.7	1.39R

On the basis of the ICP-MS-derived compositions, the configurational entropy (ΔS) was quantitatively evaluated according to the Boltzmann formalism[4]

$$\Delta S = -R\sum_{i=1}^{n} x_i \ln x_i \quad (1)$$

where x_i the atomic fraction of the i element and R the gas constant. The FeCoNiCuZnAl-LDH exhibited a ΔS value of 1.70R, unequivocally satisfying the thermodynamic criterion for classification as a high-entropy material (HEM). In contrast, the analogous calculations unveiled progressively reduced entropy of 1.57R for FeCoNiZnAl-LDH and FeNiCuZnAl-LDH, and 1.38R for FeNiZnAl-LDH, as displayed in Table S1. This entropy gradient revealed a systematic diminution in

configurational disorder with decreasing elemental diversity, which in turn implicated a reduced entropy-driven stabilization effect.

The implications of such entropy stabilization were multifold. First, the elevated ΔS disclosed for FeCoNiCuZnAl-LDH was anticipated to suppress mitigate phase segregation under thermal or electrochemical perturbations, thereby reinforcing structural robustness. Second, the coexistence of multiple cationic species with diverse electronic configurations and ionic radii was expected to modulate the electronic band manifold, revealing the potential for broadened optical absorption profiles and facilitating multi-channel charge transport pathways. Finally, the entropic contribution to stabilization illustrated an intrinsic design principle for tailoring LDH-based frameworks toward synergistically enhanced optoelectronic functionality and long-term operational stability.

S1-4 GIWAXS and GISAXS investigations of LDHs

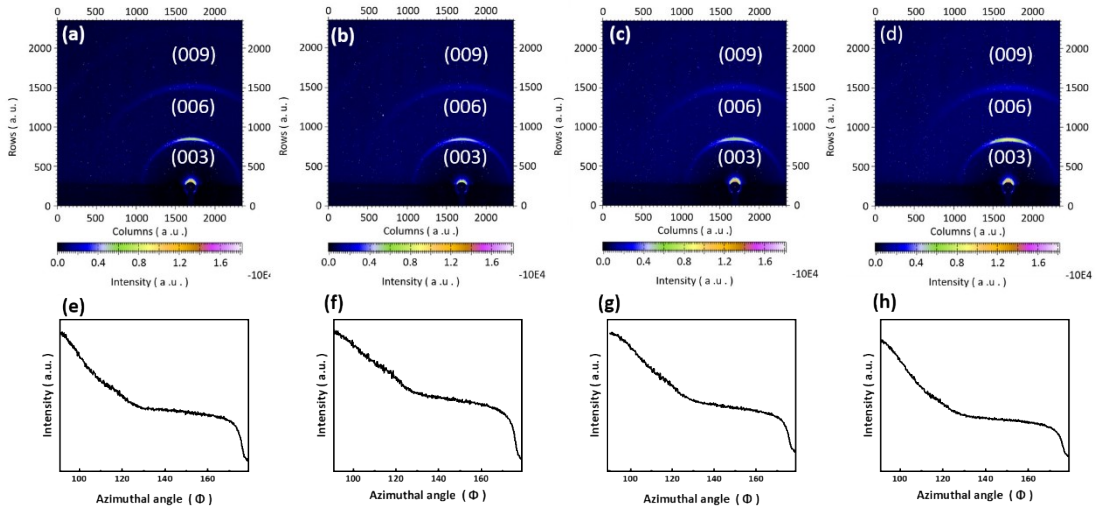

Fig. S6 Analytic GIWAXS profiles of (a) FeCoNiCuZnAl-LDH, (b) FeCoNiZnAl-LDH, (c) FeNiCuZnAl-LDH, (d) FeNiZnAl-LDH and normalized intensity–azimuth curve of (e) FeCoNiCuZnAl-LDH, (f) FeCoNiZnAl-LDH, (g) FeNiCuZnAl-LDH, (h) FeNiZnAl-LDH, respectively.

The azimuthal coordinate was defined as the angular separation between the projected scattering vector and the in-plane q_{xy} axis. A perfectly vertical platelet alignment corresponds to growth along the normal of the (113) basal plane, which geometrically manifested as a preferential azimuthal maximum of the (003) reflection at 90°. The normalized intensity–azimuth plots, as displayed in Figs. S6(e)–S6(h), disclosed a markedly suppressed baseline intensity between 130° and 170°. This suppression implicated a diminished fraction of randomly oriented crystallites, thereby uncovering the emergence of a well-defined preferential alignment.

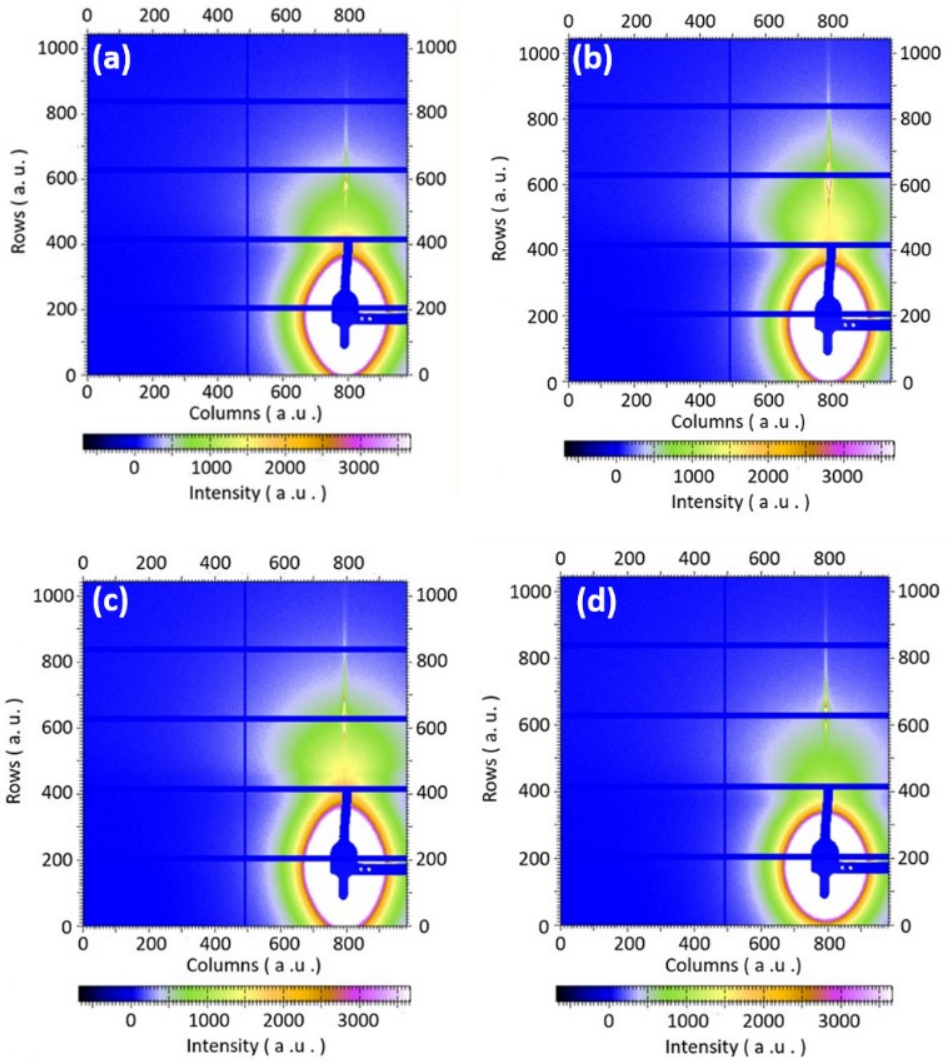

Fig. S7 Analytic GISAXS profiles of (a) FeCoNiCuZnAl-LDH, (b) FeCoNiZnAl-LDH, (c) FeNiCuZnAl-LDH, (d) FeNiZnAl-LDH, respectively.

S1-4 Surface chemical characterizations

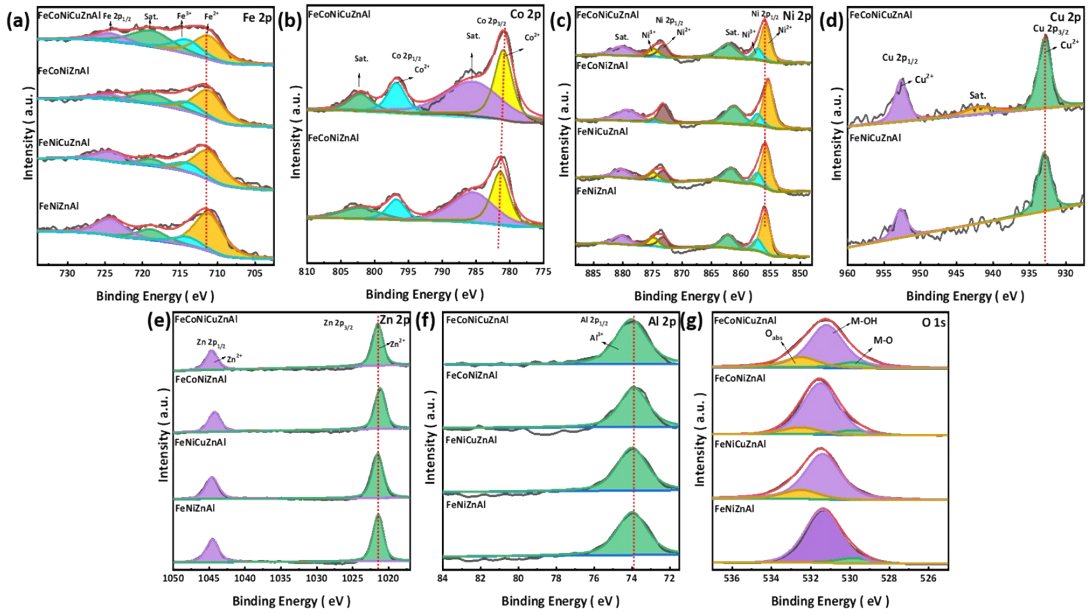

Fig. S8 High-resolution XPS spectra (a) Fe 2p, (b) Co 2p, (c) Ni 2p, (d) Cu 2p, (e) Zn 2p, (f) Al 2p, and (g) O 1s of FeCoNiCuZnAl-LDH, FeCoNiZnAl-LDH, FeNiCuZnAl-LDH, and FeNiZnAl-LDH, respectively.

Fe 2p spectrum was presented in Fig. S8(a), where two dominant spin–orbit peaks were resolved at 714.4 eV (Fe $2p_{3/2}$) and 724.2 eV (Fe $2p_{1/2}$), accompanied by a characteristic satellite at ~718.8 eV, were indicated. Deconvolution of the Fe $2p_{3/2}$ envelope uncovered distinct Fe^{2+} (711.2 eV) and Fe^{3+} (714.05 eV) contributions[5], visualizing a mixed-valence configuration that was pivotal for charge compensation and structural stabilization within the LDH lattice. Co 2p spectrum revealed in Fig. S8(b), illustrating that Co $2p_{3/2}$ and Co $2p_{1/2}$ peaks, located at 798.3 eV and 781.4 eV, respectively, corresponded to Co^{2+}. The pronounced shake-up satellites at 785.4 eV and 802.1 eV disclosed the many-body effects inherent to Co 2p transitions, thereby reinforcing the divalent assignment[6] . Ni 2p spectrum was shown in Fig. S8(c). Mixed valence features were evident, with Ni^{2+} peaks at 855.9 eV ($2p_{3/2}$) and 873.2 eV ($2p_{1/2}$),

and Ni^{3+} components at 857.2 eV and 874.8 eV. Associated satellite structures at ~862.2 eV and ~880.3 eV further corroborated the coexistence of Ni^{2+}/Ni^{3+} states, consistent with prior reports on Ni-based LDHs[7] . Cu 2p spectrum was displayed in Fig. S8(d). The Cu $2p_{3/2}$ (933.0 eV) and Cu $2p_{1/2}$ (953.2 eV) featured corresponded to Cu^{2+}, while a satellite at ~942.0 eV provided additional evidence of the divalent oxidation state. Zn 2p spectrum was illustrated in Fig. S8(e). A well-defined doublet at 1021.5 eV ($2p_{3/2}$) and 1044.6 eV ($2p_{1/2}$) confirmed that Zn ions persist stably in a divalent state within the LDH lattice. Al 2p spectrum was featured in Fig. S8(f). A sharp feature at 73.9 eV corresponded to Al^{3+}, implicating the successful incorporation of trivalent aluminum into the layered framework without valence fluctuation. O 1s spectrum was presented in Fig. S8(g), where three distinct components were visualized: 529.8 eV (lattice M–O bonds), 531.4 eV (hydroxyl groups, M–OH), and 533.3 eV (adsorbed oxygen, O_{ads}). The dominance of the M–OH contributions from all tested samples illustrated the retention of hydroxyl functionality, which was indispensable for LDH structures and substantiates the integrity of the synthesized structure.

S1-5 Size distribution of synthesized LDHs

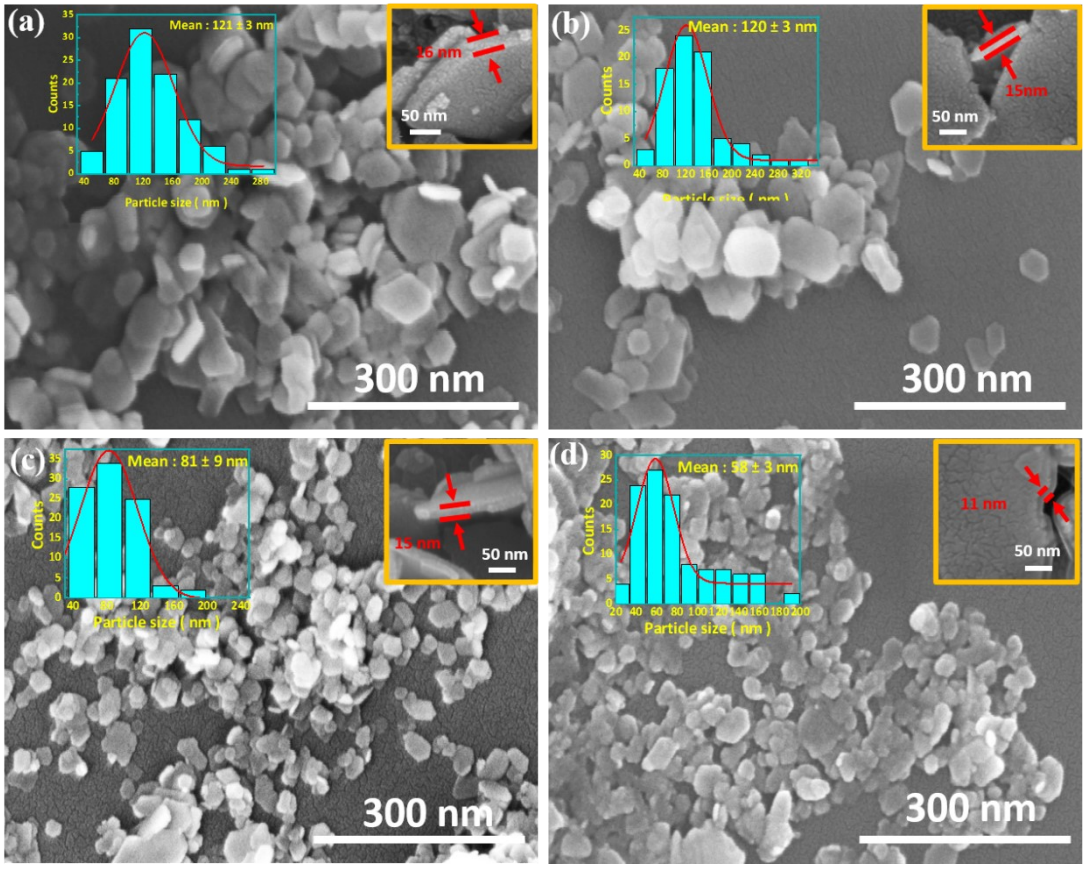

Fig. S9 Top-view SEM images of (a) FeCoNiCuZnAl-LDH, (b) FeCoNiZnAl-LDH, (c) FeNiCuZnAl-LDH, (d) FeNiZnAl-LDH, respectively. In addition, size distributions and layer thickness obtained from SEM observations were shown in the insets, respectively.

Quantitative analysis disclosed that the mean lateral sizes of FeCoNiCuZnAl, FeCoNiZnAl, FeNiCuZnAl, and FeNiZnAl were 121±3 nm, 120±3 nm, 81±9 nm, and 58±3 nm, respectively. Such variation in nanosheet size could be understood by configurational entropy effects in conjunction with ion-specific lattice regulation. In addition to entropy considerations, disparities in ionic radii and the coordination preferences of transition-metal cations inevitably induced the lattice perturbations, which directly modulated the growth kinetics and govern the

ultimate nanosheet dimensions. In particular, FeCoNiCuZnAl-LDH demonstrated the most pronounced in-plane growth, wherein the simultaneous incorporation of Co and Cu was inferred to lower the surface energy of specific facets while reinforcing overall lattice stability. Interestingly, the FeCoNiZnAl-LDH sample, despite lacking Cu constitutes, displayed the comparable lateral extension, thereby implicating Co constitutes as the dominant driving factor for causing the nanosheet growth.

S1-6 Characteristic UPS spectra of LDHs

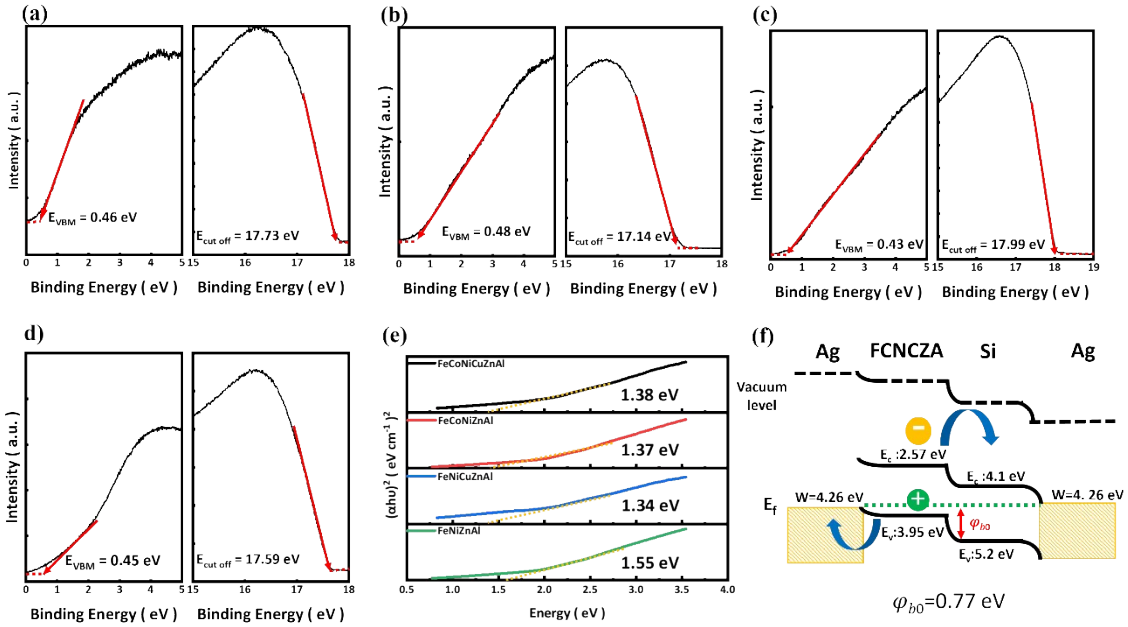

Fig. S10 Analytic UPS spetra of (a) FeCoNiCuZnAl-LDH, (b) FeCoNiZnAl-LDH, (c) FeNiCuZnAl-LDH, (d) FeNiZnAl-LDH, respectively. (e) Tauc plot-derived optical bandgap determination,. (f) Band diagrams of heterojunction created between LDH structures and Si.

S2 Optoelectronic characterizations

S2-1 Optoelectronic characterizations of LDH/bulk Si heterostructures

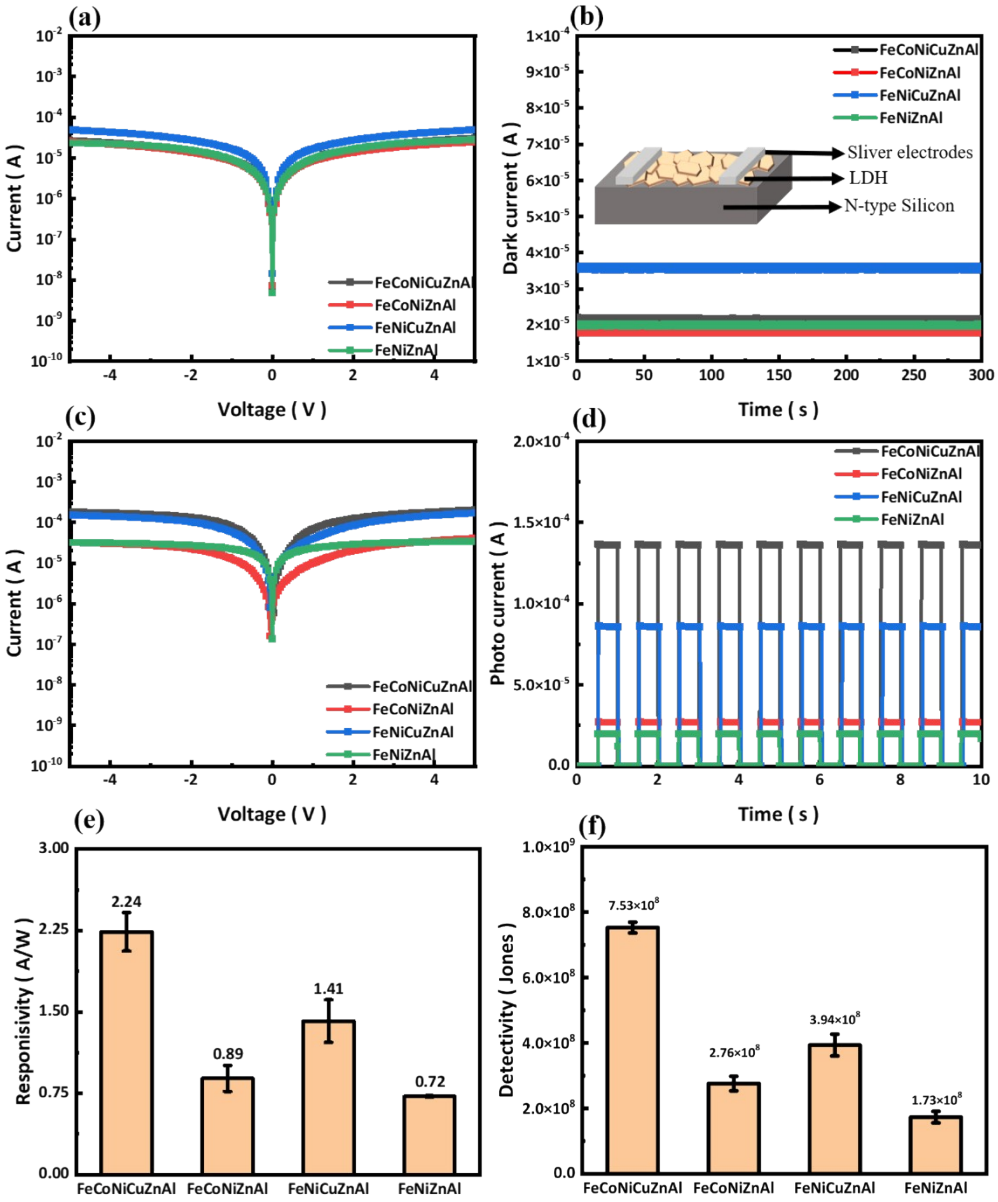

Fig. S11 (a) Dark I-V curves, (b) time-dependent dark current curves, (c) I-V curves under the light illuminations of 940 nm (d) optical on–off switch photoresponse, (e)Responsivity, and (f) Detectivity of LDH/Bulk Si. The error bars represented 5 independently measured cycles per time point, with relative standard deviations of ±9.4%.

As indicated in Fig. S11(a), the I–V characteristics of LDH/bulk Si heterojunctions under dark conditions were visualized. A pronounced saturation trend was disclosed when the applied bias exceeds +3 V. Fig. S11(b) demonstrated the time-resolved dark current (I–t) curves measured at +3 V, where the FeCoNiCuZnAl-LDH/bulk Si, FeCoNiZnAl-LDH/bulk Si, FeNiCuZnAl-LDH/bulk Si, and FeNiZnAl-LDH/bulk Si devices revealed stable dark currents of 21.6, 18.0, 35.7, and 19.7 μA, respectively. The distinct features could be interpreted by the following considerations. First, Cu^{2+}, with its relatively low impedance and high 3d electron density, uncovered a propensity to capture environmental oxygen, which caused the extrinsic hole injection into the Si substrates. Among them, the FeNiCuZnAl-LDH/Bulk Si device demonstrated the lowest dark current due to the of Cu^{2+} constitutes. Next, in the FeCoNiCuZnAl system, the configurational entropy effect unveiled a statistical redistribution of Cu^{2+} adsorption sites. Such dispersion effectively screened th effect of localized hole injection, thereby suppressing the augment of dark current. Fig. S11(c) displayed the I-V curves of various device under 940-nm light illuminations, respectively, and the corresponding transient photocurrents under chopped 940 nm irradiation (4 mW cm^{-2}, 1 Hz, +3 V bias) were illustrated in Fig. S11(d). The results disclosed that FeCoNiCuZnAl-LDH/bulk Si, FeCoNiZnAl-LDH/bulk Si, FeNiCuZnAl-LDH/bulk Si, and FeNiZnAl-LDH/bulk Si devices exhibited photocurrents of 135, 53, 85, and 43 μA, respectively. The calculated responsivities were 2.24±0.18, 0.89±0.09, 1.41±0.13, and 0.72±0.01 A W^{-1} for FeCoNiCuZnAl-LDH/bulk Si, FeCoNiZnAl-LDH/bulk Si, FeNiCuZnAl-LDH/bulk Si, and FeNiZnAl-LDH/bulk Si photodetectors, respectively. In addition, the revealed detectivities

were $7.53\pm0.16\times10^{8}$, $2.76\pm0.22\times10^{8}$, $3.94\pm0.33\times10^{8}$, and $1.73\pm0.18\times10^{8}$ Jones, respectively. The markedly superior performance of the FeCoNiCuZnAl device uncovered the crucial role of entropy-stabilized lattice configurations in mitigating extrinsic Cu^{2+}-induced noise channels while simultaneously enhancing photon-to-electron conversion efficiency.

S2-2 Optoelectronic characterizations of LDH/SiNW heterostructures

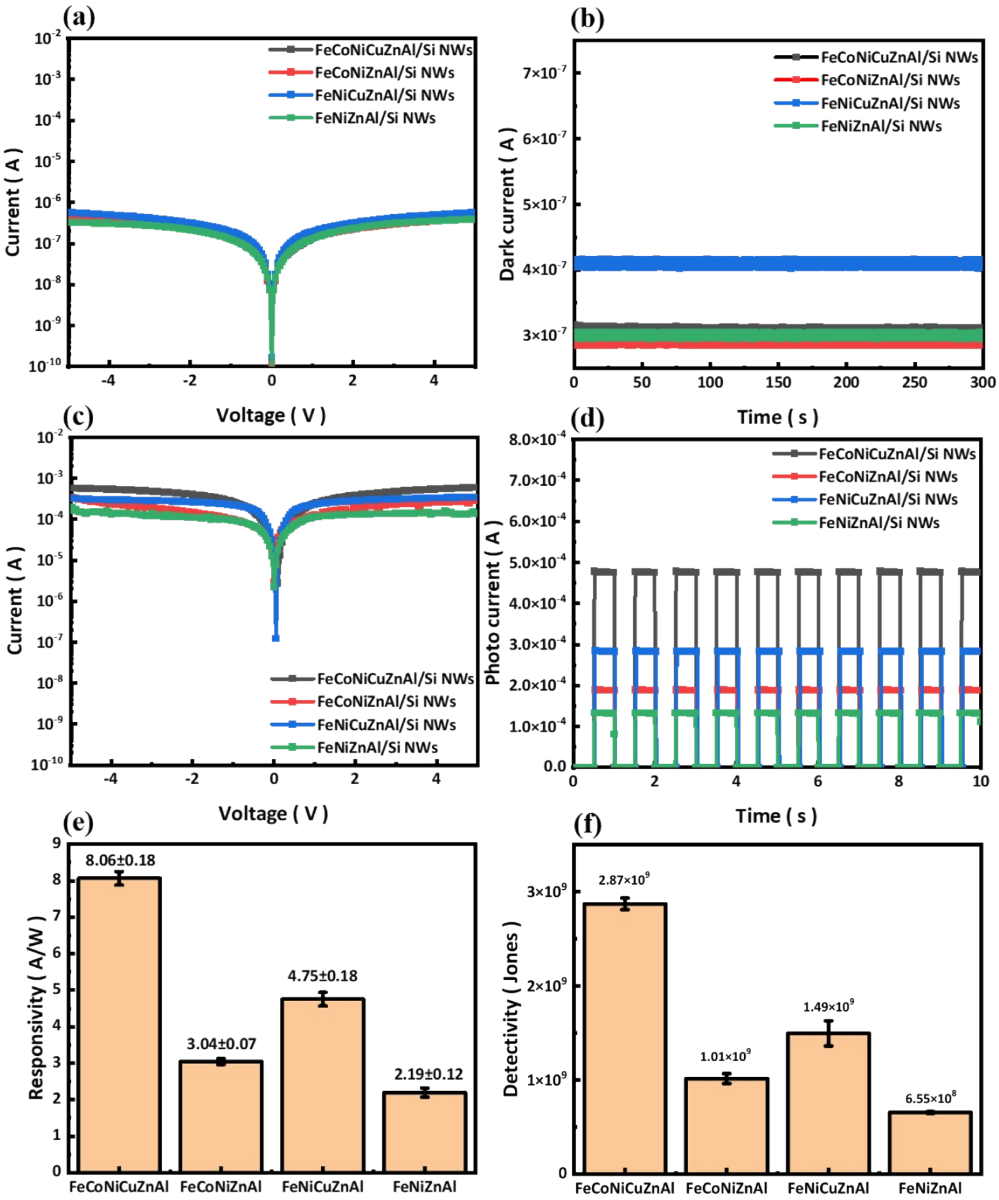

Fig. S12 (a) Dark I-V curve, (b) the time-dependent dark current, curve (c) I-V curve under the light illuminations of 940 nm (d) optical on–off switch photoresponses, (e)Responsivity, and (f) Detectivity of LDH/Si NWs. The error bars represented 5 independently measured cycles per time point, with relative standard deviations of ±4.9%.

Figs. S12(a) and S12(b) illustrated the measured I-V results and temporal dark current (I–t) responses at +3 V, respectively. The results revealed that FeCoNiCuZnAl-LDH/Si NWs, FeCoNiZnAl-LDH/Si NWs, FeNiCuZnAl-LDH/Si NWs, and FeNiZnAl-LDH/Si NWs devices presented the stabilized dark currents of 310, 293, 415, and 305 nA, respectively. Fig. S12(d) demonstrated the dynamic photocurrent (I–t) traces at +3 V bias under modulated 940-nm light irradiations (4 mW cm^{-2}, 1 Hz). Quantitative analysis disclosed photocurrents of 482, 188, 283, and 133 μA from FeCoNiCuZnAl-LDH/Si NWs, FeCoNiZnAl-LDH/Si NWs, FeNiCuZnAl-LDH/Si NWs and FeNiZnAl-LDH/Si NWs devices, respectively. To further elucidate optoelectronic performance, the responsivity values were extracted [Fig. S12 (e)]. The corresponding responsivities are 8.04±0.18, 3.13±0.08, 4.72±0.19, and 2.21±0.13 A W^{-1} for the four devices, respectively. Fig. S12(f) featured the specific detectivities, where the FeCoNiCuZnAl-LDH/Si NWs, FeCoNiZnAl-LDH/Si NWs, FeNiCuZnAl-LDH/Si NWs and FeNiZnAl-LDH/Si NWs photodetectors revealed detectivities of $2.87\pm0.06\times10^{9}$, $1.01\pm0.05\times10^{9}$, $1.49\pm0.13\times10^{9}$, and $6.55\pm0.10\times10^{8}$Jones, respectively.

S2-3 Photodetection selectivity of FeCoNiCuZnAl-LDH/SiNW heterostructures

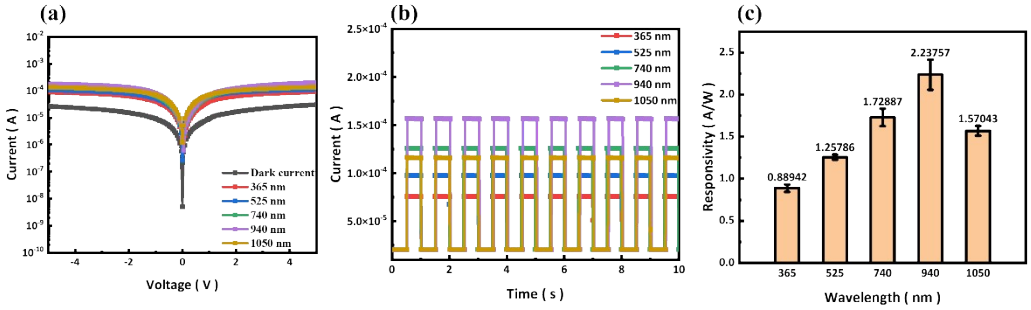

Fig. S13 (a) I-V curve, (b) on/off switching photoresponse, and (c) responsivity of FeCoNiCuZnAl-LDH/SiNW under the light illumination of five various wavelengths, respectively. The results revealed the obtained photocurrents of 0.89 ± 0.04 AW^{-1}, 1.26 ± 0.03 AW^{-1}, 1.73 ± 0.10 AW^{-1}, 2.24 ± 0.18 AW^{-1}, and 1.57 ± 0.06 AW^{-1} from the irradiated light wavelengths of 365, 525, 740, 940, and 1050 nm, respectively. The error bars represented 5 independently measured cycles per time point, with relative standard deviations of ±7.8%.

S2-4 Optoelectronic characterizations of FeCoNiCuZnAl-LDH/Bulk Si and FeCoNiCuZnAl-LDH/Si NWs heterostructures

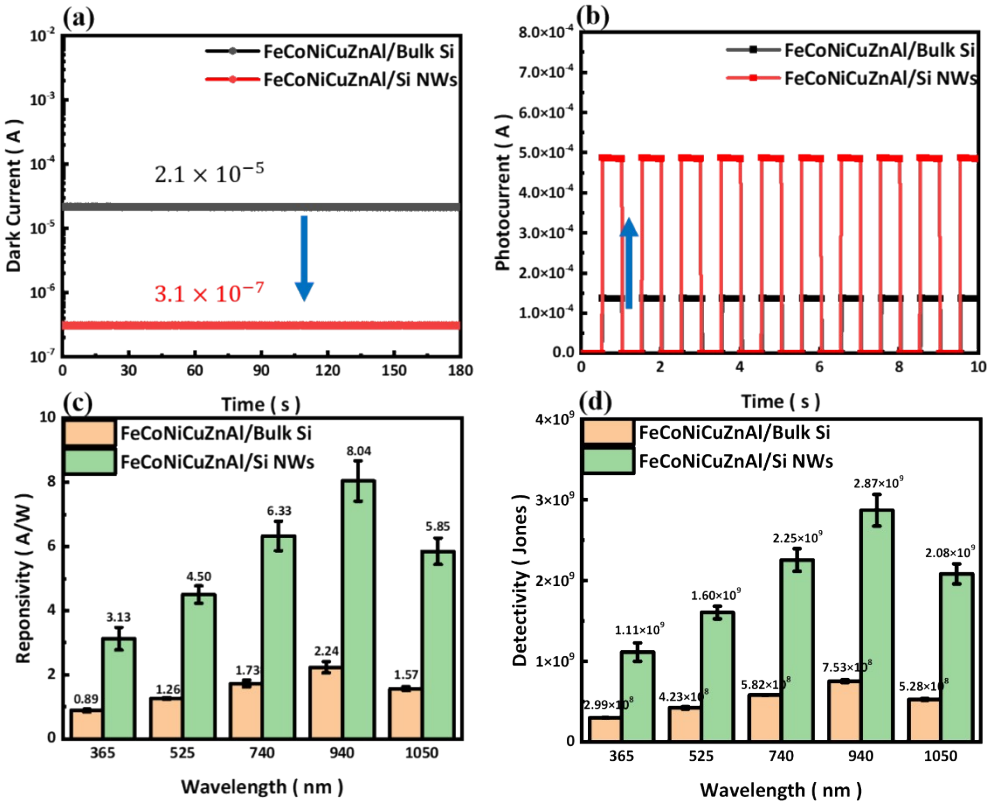

Fig. S14 (a) On/off switching photoresponse, (b) time-dependent dark currents, (c) responsivity, and (d) detectivity of FeCoNiCuZnAl-LDH/Bulk Si and FeCoNiCuZnAl-LDH/SiNW. The error bars represented 5 independently measured cycles per time point, with relative standard deviations of ±7.9%.

S3 Characteristics of LDHs after post anneal treatment

S3-1 GIWAXS and GISAXS profiles of LDHs after annealing

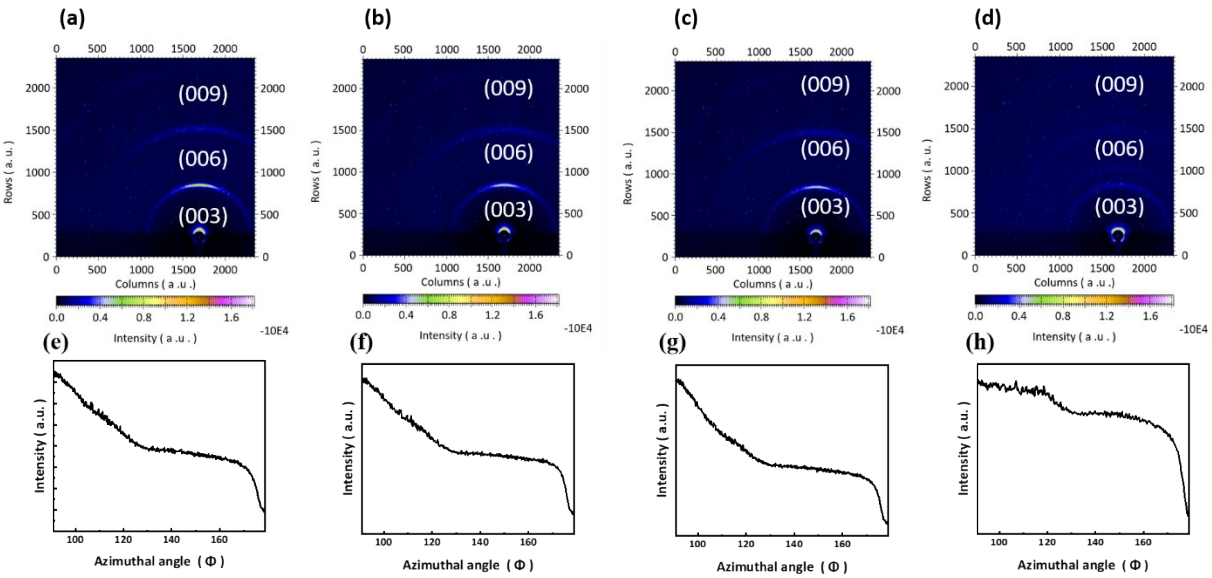

Fig. S15 Analytic GIWAXS profiles of (a)Pristine, (b) anneal at 85°C, (c) anneal at 100°C and (d) anneal at 115°C, respectively. The normalized intensity–azimuth curve of (e)pristine, (f) anneal at 85°C, (g) anneal at 100°C, (h) anneal at 115°C of FeCoNiCuZnAl-LDH, respectively

This narrowing of the azimuthal intensity distribution could be interpreted as follows: First, removal of interlayer water adsorbents and volatile species improved the structuring ordering in layered features, thereby allowing entropic stabilization of ordered platelets. Next, the anneal procedures mediated the stress released at LDH/substrate interfaces, which implicated more coherent stacking along the c-axis and in turn sharpened Bragg features. Finally, the progressive dehydroxylation and redistribution of hydrogen bonds promoted more ordered gallery heights. These combined effects manifested the reduced azimuthal background and intensification of (003) spots.

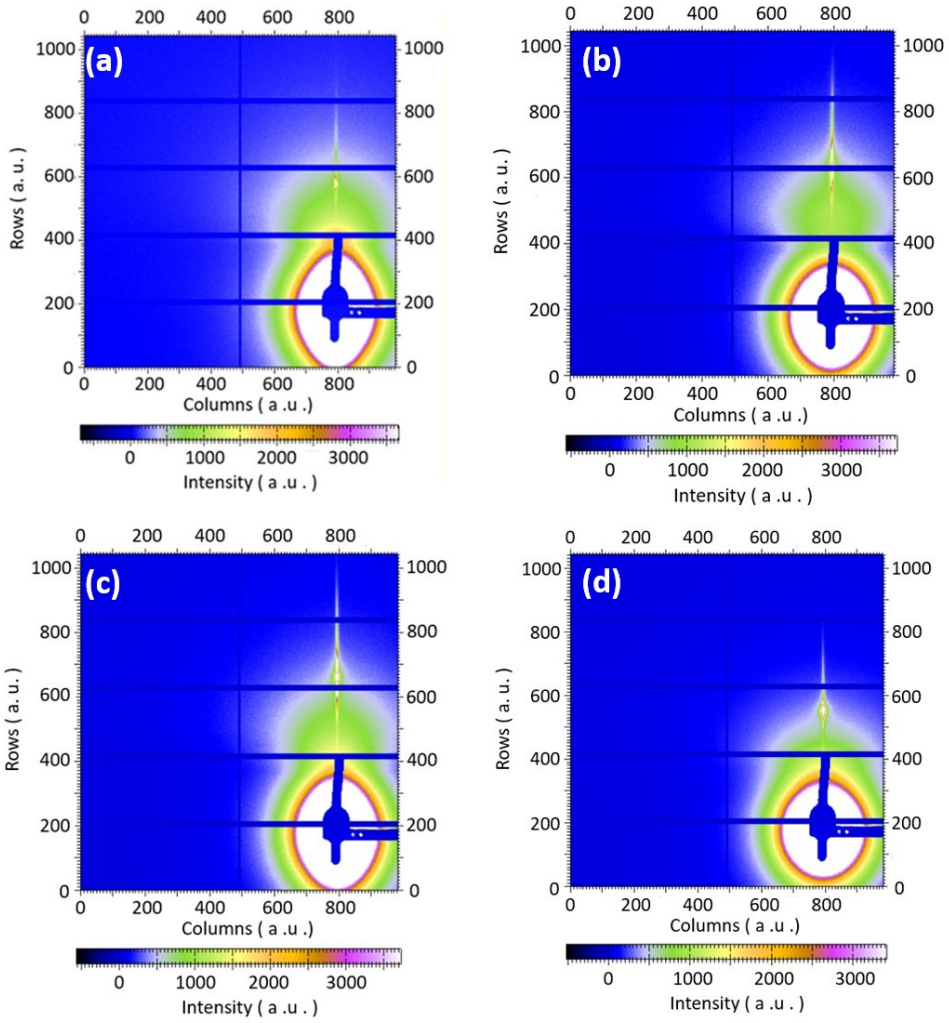

Fig. S16 Analytic GISAXS profiles of (a) pristine, (b) anneal at 85°C, (c) anneal at 100°C, (d) anneal at 115°C of FeCoNiCuZnAl-LDH, respectively.

S3-2 XRD patterns of synthesized LDHs

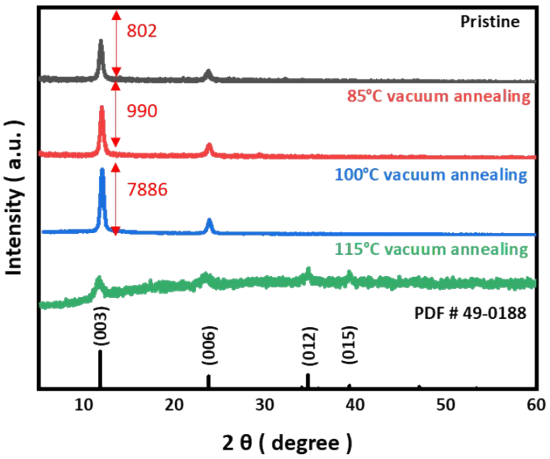

Fig. S17 XRD patterns of FeCoNiCuZnAl-LDH after undergoing post anneal with different temperatures, respectively.

S3-3 Surface chemical characterizations

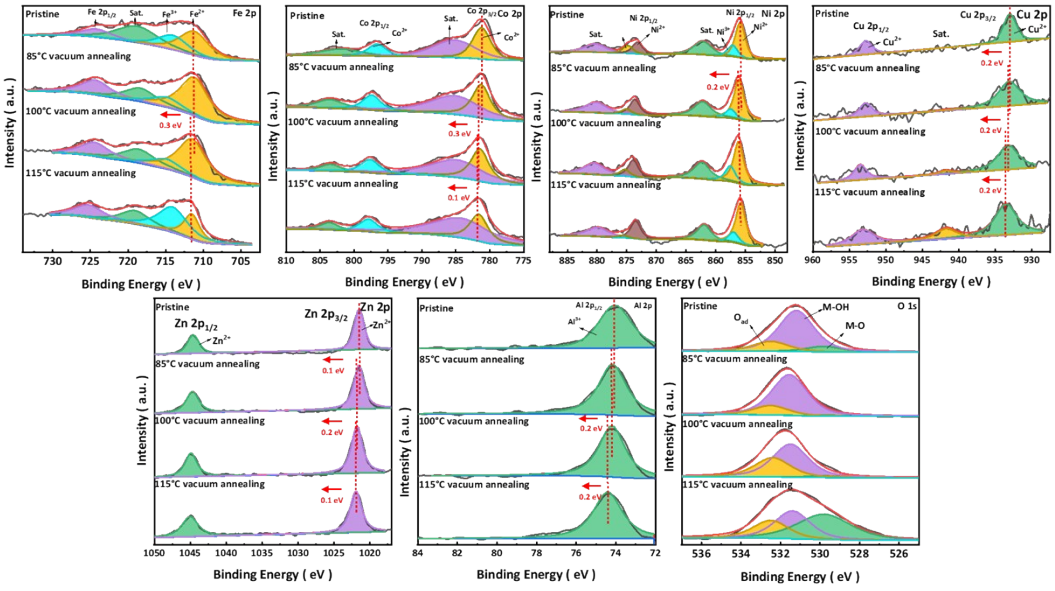

Fig. S18 High-resolution XPS spectra (a) Fe 2p, (b) Co 2p, (c) Ni 2p, (d) Cu 2p, (e) Zn 2p, (f) Al 2p, and (g) O 1s of as-annealed FeCoNiCuZnAl-LDH, respectively.

All constituent metal cations exhibited a systematic positive shift in binding energy, ranging from 0.1 to 0.6 eV. This monotonic upshift could be understood by two

interrelated mechanisms. First, in pristine LDHs, the M–OH coordination involved hydroxyl ligands with relatively high electronegativity and localized lone pairs, which contribute partial electron density to the metal center through covalent or partially ionic bonding. Upon annealing, the scission of M–OH moieties and the subsequent generation of terminal oxo (M=O) or bridging M–O–M linkages diminished this electron donation. The resulting reduction of valence electron density around the metal cores enhanced the effective electrostatic attraction exerted by the nuclei. Consequently, the core electrons were more tightly bound, manifesting as an upshift in the XPS binding energies. Next, the involvement of hydroxyl groups acting as electron-donating ligands, partially screened the nuclear potential of the coordinated metal cations. In contrast, the transformation into bridging M–O–M motifs redistributed the oxygen electronic density across two adjacent metal centers, thereby weakening the local shielding effect. The diminished screening further increased the effective nuclear charge felt by the core electrons, again shifting the measured binding energy to higher values. This overall electronic reorganization was corroborated by the O 1s spectra. Initially, the hydroxyl component dominated the O 1s envelope, accounting for ~85% of the total signal. With incremental annealing, however, the M–OH contribution progressively decreased to 81% at 85°C, 61% at 100°C, and ultimately only 33% at 115°C. In parallel, the relative fraction of adsorbed oxygen (O_{ads}) raised substantially from 11% in the pristine state to 36% after conducting anneal process.

S4 Optoelectronic analyses after post anneal

S4-1 Optoelectronic characterizations of annealed-FeCoNiCuZnAl-LDH/SiNW

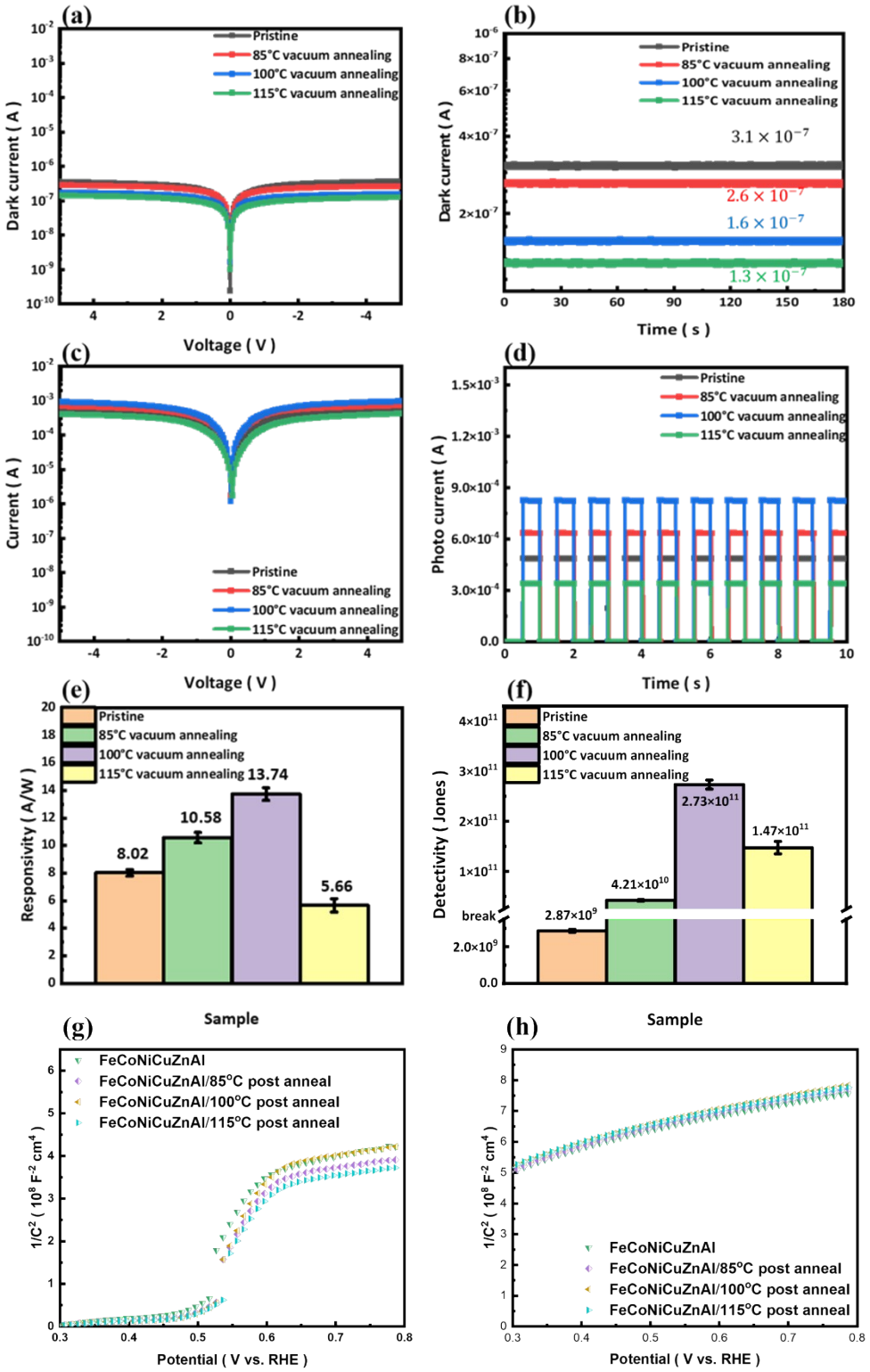

Fig. S19 (a) Dark I-V, (b) time-dependent dark current, (c) I-V under light illuminations of 940 nm, (d) on/off switch photoresponses, (e) responsivity, and (f) detectivity of annealed FeCoNiCuZnAl-LDH/SiNW. The error bars represented 3 independently measured cycles per time point, with relative standard deviations of ±7.4%. Mott

Schottky plots at (g) low frequencies (1 Hz) and (h) high frequencies (1000 Hz) of FeCoNiCuZnAl-LDH after annealing at 85 °C, 100 °C and 115 °C, respectively.

The measurements were performed in 1 M KOH electrolyte using an AC perturbation of 10 mV within 0.3–0.8 V (vs RHE) to exclude the flat-band region (< 0.2 V). At 1000 Hz [Fig. S19h], the $1/C^2$–V profiles of all annealed samples nearly overlap, confirming that the high-frequency response was dominated by depletion-layer capacitance. In contrast, at 1 Hz [Fig. S19g], the pristine device exhibited a pronounced low-bias capacitance enhancement associated with slow interfacial-trap charging, which was progressively suppressed after undergoing the anneal process. The sample annealed at 100 °C displayed a nearly linear depletion behavior across 0.3–0.8 V. This evolution indicated a significant reduction of interfacial-trap states due to the reconstruction of M–OH sites into bridging M=O/M–O–M linkages. These electrochemical results corroborated the results of flicker-noise reduction observed in Fig. 4(c) of the main text.

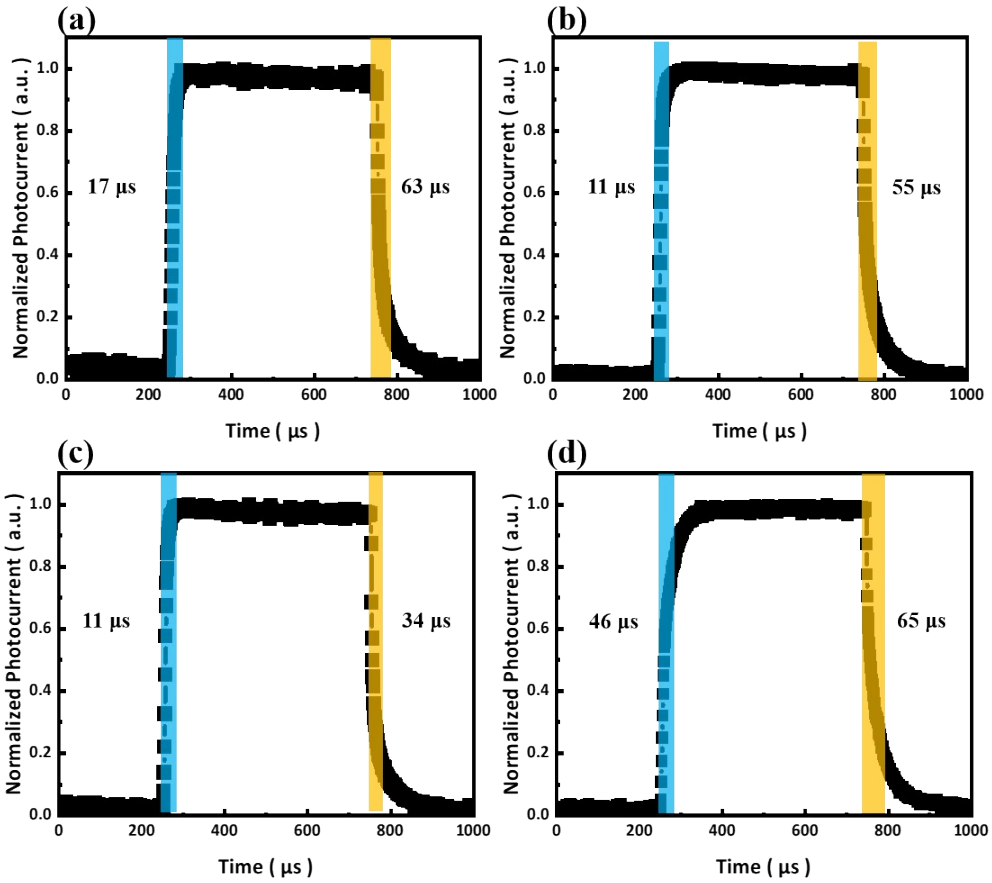

Fig. S20 Rising time and fall time of (a) pristine, (b) 85°C anneal, (c) 100°C anneal, (d) 115°C anneal from FeCoNiCuZnAl-LDH.

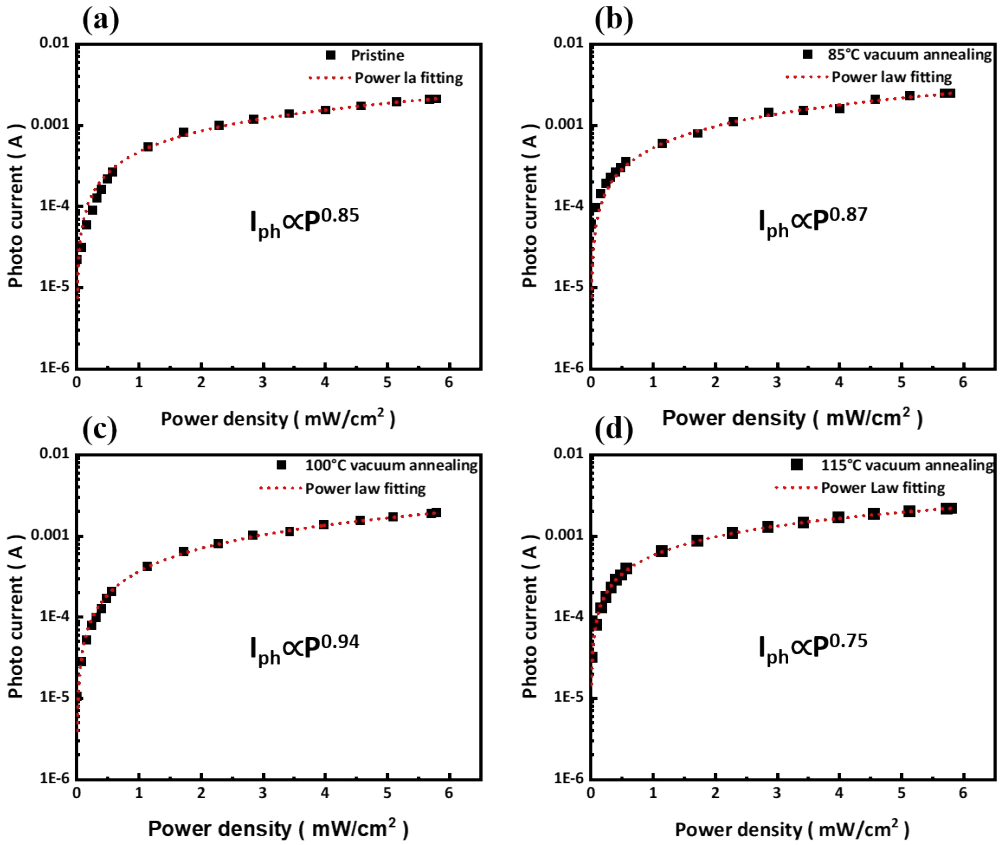

Fig. S21 Light-power dependent photoresponses and correlated power-Law fitting of (a) pristine, (b) 85°C anneal (c) 100°C anneal, (d) 115°C anneal from FeCoNiCuZnAl-LDH.

The correlation between photocurrent (I_{ph}) and incident optical power density (P) could be quantitatively described by a power-law dependence:

$$I_p = CP^{\theta} \quad (2)$$

where C a wavelength-dependent proportionality constant, and θ the retrieval parameter that characterized the degree of linearity between the incident photon flux and the generated photocurrent. Accordingly, the extracted θ values from the pristine device and those subjected to vacuum anneal at 85°C, 100°C, and 115°C were 0.85, 0.87, 0.94, and 0.75, respectively.

Table S2 Performance comparisons with state-of-art NIR photodetectors

Material	λ (nm)	R (mA/W)	D* (Jones)	EQE (%)	Rising time	Recovery time	f_{-3dB} (Hz)	Flicker noise ($A*Hz^{-1/2}$)	Reference
(FeNiCoMnMgCu)Ox	365-1050	3500	4.6×10^{13}	732	126 µs	811 µs	NA	$\sim10^{-10}$	8
PbS:P3HT:PCBM:ZnO	930	1240	2.66×10^{11}	166	160 µs	80 µs	NA	**$\sim10^{-11}$**	9
MoO_3/InAs/ZnO	940	220	10^{11}	30	2 ns	2 ns	150 M	NA	10
Bi_2S_3	940	0.75	2.69×10^{9}	NA	61 ms	180 ms	NA	NA	11
Si/SiOx/ZrO_2	940	3400	1.2×10^{10}	NA	2 µs	4 µs	NA	$\sim10^{-11}$	12
Bi_2O_2Se	940	~6.28	$\sim4.1\times10^{8}$	NA	167 ms	357 ms	NA	NA	13
MoS_2/Pt	940	15000	2.09×10^{12}	NA	64.3 ms	53.6 ms	NA	NA	14
InAs CQD	940	600	3.1×10^{11}	79	46 ns	76 ns	NA	NA	15
Cu-Cu_2O/ZnO	940	0.06153	4.07×10^{8}	NA	19.07 ms	27.28 ms	NA	NA	16
FeCoNiCuZnAl-LDH/SiNW	940	13740	2.73×10^{1}	1812	11 µs	34 µs	30k	3.1×10^{-13}	This work

References

1. B. S. Yadav and S. Dasgupta, *Inorganic Chemistry Communications*, 2022, **137**, 109203.
2. A. M. Thomas, C. Yoon, S. Ippili, V. Jella, T.-Y. Yang, G. Yoon and S.-G.

Yoon, *ACS Applied Materials & Interfaces*, 2021, **13**, 61434-61446.
3. S.-L. Wang and P.-C. Wang, *Colloids and Surfaces A: Physicochemical and Engineering Aspects*, 2007, **292**, 131-138.
4. S. S. Aamlid, M. Oudah, J. Rottler and A. M. Hallas, *Journal of the American Chemical Society*, 2023, **145**, 5991-6006.
5. C. Pitchai and C.-M. Chen, *Sustainable Energy & Fuels*, 2025, **9**, 1829-1838.
6. S. Chen, Q. Yang, J. Shi, Y. Ying and Y. Liu, *Colloids and Surfaces A: Physicochemical and Engineering Aspects*, 2022, **635**, 128078.
7. Y. Zhai, X. Ren, T. Gan, L. She, Q. Guo, N. Yang, B. Wang, Y. Yao and S. Liu, *Advanced Energy Materials*, 2025, 2502065.
8. C.-Y. Chen, J.-Y. Li, K.-Y. Kuo, T. X. Nguyen, P.-H. Hsiao and J.-M. Ting, *ACS Applied Materials & Interfaces*, 2023, **15**, 52716-52723.
9. R. Dong, C. Bi, Q. Dong, F. Guo, Y. Yuan, Y. Fang, Z. Xiao and J. Huang, *Advanced Optical Materials*, 2014, **2**, 549-554.
10. B. Sun, A. M. Najarian, L. K. Sagar, M. Biondi, M. J. Choi, X. Li, L. Levina, S. W. Baek, C. Zheng and S. Lee, *Advanced Materials*, 2022, **34**, 2203039.
11. P. Rong, S. Gao, S. Ren, H. Lu, J. Yan, L. Li, M. Zhang, Y. Han, S. Jiao and J. Wang, *Advanced Functional Materials*, 2023, **33**, 2300159.
12. N. E. Silva, A. R. Jayakrishnan, A. Kaim, K. Gwozdz, L. Domingues, J. Kim, M. C. Istrate, C. Ghica, M. Pereira and L. Marques, *Advanced Functional Materials*, 2025, **35**, 2416979.
13. S. Ren, S. Gao, P. Rong, L. Li, M. Zhang, H. Lu, J. Yan, D. Ling, S. Jiao and J. Wang, *Chemical Engineering Journal*, 2023, **468**, 143626.
14. M. Dai, Q. Wu, C. Wang, X. Liu, X. Zhang, Z. Cai, L. Lin, X. Gu, K. Ostrikov and H. Nan, *Advanced Optical Materials*, 2024, **12**, 2301900.
15. D. Shin, H. Jeong, J. Kim, E. Jang, Y. Park and S. Jeong, *Advanced Optical Materials*, 2025, **13**, 2401931.
16. A. K. Rana, J. T. Park, J. Kim and C.-P. Wong, *Nano Energy*, 2019, **64**, 103952.